

THE DYNAMICS OF MASSIVE STARLESS CORES WITH ALMA

JONATHAN C. TAN

Departments of Astronomy & Physics, University of Florida, Gainesville, FL 32611, USA

SHUO KONG, MICHAEL J. BUTLER

Department of Astronomy, University of Florida, Gainesville, FL 32611, USA

PAOLA CASELLI

School of Physics & Astronomy, The University of Leeds, Leeds, LS2 9JT, UK

FRANCESCO FONTANI

INAF - Osservatorio Astrofisico di Arcetri, Largo Enrico Fermi 5, I - 50125 Firenze, Italy

Accepted to the Astrophysical Journal on 31st Oct. 2013

ABSTRACT

How do stars that are more massive than the Sun form, and thus how is the stellar initial mass function (IMF) established? Such intermediate- and high-mass stars may be born from relatively massive pre-stellar gas cores, which are more massive than the thermal Jeans mass. The Turbulent Core Accretion model invokes such cores as being in approximate virial equilibrium and in approximate pressure equilibrium with their surrounding clump medium. Their internal pressure is provided by a combination of turbulence and magnetic fields. Alternatively, the Competitive Accretion model requires strongly sub-virial initial conditions that then lead to extensive fragmentation to the thermal Jeans scale, with intermediate- and high-mass stars later forming by competitive Bondi-Hoyle accretion. To test these models, we have identified four prime examples of massive ($\sim 100 M_{\odot}$) clumps from mid-infrared extinction mapping of infrared dark clouds (IRDCs). Fontani et al. found high deuteration fractions of N_2H^+ in these objects, which are consistent with them being starless. Here we present ALMA observations of these four clumps that probe the $N_2D^+(3-2)$ line at $2.3''$ resolution. We find six N_2D^+ cores and determine their dynamical state. Their observed velocity dispersions and sizes are broadly consistent with the predictions of the Turbulent Core model of self-gravitating, magnetized (with Alfvén Mach number $m_A \sim 1$) and virialized cores that are bounded by the high pressures of their surrounding clumps. However, in the most massive cores, with masses up to $\sim 60 M_{\odot}$, our results suggest that moderately enhanced magnetic fields (so that $m_A \simeq 0.3$) may be needed for the structures to be in virial and pressure equilibrium. Magnetically regulated core formation may thus be important in controlling the formation of massive cores, inhibiting their fragmentation, and thus helping to establish the stellar IMF.

Subject headings: ISM: clouds, dust, extinction — stars: formation

1. INTRODUCTION

The two main theories for massive (and intermediate-mass) star formation, Core Accretion (e.g. McLaughlin & Pudritz 1996; McKee & Tan 2003, hereafter MT03) and Competitive Accretion (e.g. Bonnell et al. 2001; Wang et al. 2010), invoke very different initial conditions for the gas about to collapse to form a high-mass star. The Turbulent Core Accretion model of MT03 starts with massive near-virial-equilibrium starless *cores* that will collapse to form individual stars or close binaries. These cores can be considered to be scaled-up versions of the much more common low-mass cores known to form low-mass stars (Shu et al. 1987). The main differences from low-mass cores are that the pressure support must be provided by nonthermal forms (turbulence and/or magnetic fields) and the typical environments where massive cores and stars form, self-gravitating massive *clumps* (i.e., proto-star-clusters), are at much higher pressure. Competitive Accretion also involves fragmentation of massive gas clumps, but now into protostellar seeds with initial masses only of order the thermal Jeans mass — typically much less than a solar mass under these high pressure conditions. Those protostellar seeds that happen to be in high density regions then later accrete previously unbound gas to eventually become intermediate-mass and high-mass stars. The numerical simulations of Bonnell et al. (2001), from which the competitive accretion theory was developed, involved global, near free-fall collapse of a gas clump, which either started at or evolved to a very sub-virial state. Krumholz et al. (2005) showed such a sub-virial state was needed for the competitive accretion rate to be large enough to be relevant for massive star formation, i.e. allowing formation within timescales $\lesssim 1$ Myr. Thus to distinguish between these theoretical models we need to find and measure the dynamical state of intermediate-mass and high-mass starless cores: how close are they to virial equilibrium?

Answering this question is challenging because massive starless cores are rare, typically far away, small in angular size, usually surrounded by large quantities of other molecular gas, and expected to suffer depletion of many molecular species, such as CO and CS, that are often used to measure the mass and kinematics of molecular clouds. Furthermore, it is difficult to infer the degree of support a core receives from large scale magnetic fields.

1.1. Target selection of intermediate-mass and high-mass starless cores

To find massive starless cores we started by studying infrared dark clouds (IRDCs) (e.g. Pérault et al. 1996; Egan et al. 1998) using *Spitzer* IRAC $8\mu\text{m}$ GLIMPSE survey (Benjamin et al. 2003) images. We developed a mid-infrared extinction (MIREX) mapping technique to derive mass surface densities, Σ , of clouds, probing up to $\Sigma \simeq 0.5 \text{ g cm}^{-2}$ (i.e., $N_{\text{H}} = 2.1 \times 10^{23} \text{ cm}^{-2}$) and on scales down to $2''$ (Butler & Tan 2009, hereafter BT09; Butler & Tan 2012, hereafter BT12). The method depends on the dust opacity but not the dust temperature. Figure 1a shows Σ maps of 4 core/clumps (C1, F1, F2, G2) selected from the larger sample of 42 studied by BT12. The properties of these objects are also listed in Table 1. Selection of these particular sources was guided by them having large values of Σ , still being dark at 24 and $70 \mu\text{m}$ (*Spitzer* MIPS GAL (Carey et al. 2009) images were analyzed), and being in relatively quiescent environments with respect to other star formation activity (MIR sources are absent in a $\sim 20''$ diameter aperture around the Σ peak).

1.2. CO Freeze-out and Deuterium Fractionation

In these cold ($T \sim 15 \text{ K}$; Pillai et al. 2006), high density ($n_{\text{H}} \gtrsim 10^5 \text{ cm}^{-3}$; BT12) environments, freeze-out of molecules such as CO on to dust grains is expected, as has been observed in low-mass starless cores (e.g. Caselli et al. 1999). Hernandez et al. (2011) found widespread CO depletion in the filamentary IRDC H of the BT12 sample. It has also been reported in other similar clouds by, e.g. Zhang et al. (2009) and Fontani et al. (2012). Molecules suffering freeze-out are poor tracers of starless core kinematics. However, as CO is depleted from the gas phase, the level of deuteration of certain species is expected to increase (Dalgarno & Lepp 1984). This is because CO reacts with and thus destroys H_2D^+ (that has formed by reaction of H_3^+ with HD), so when CO is depleted the concentration of H_2D^+ builds up and so deuteration of other species still present in the gas phase, such as N_2H^+ , becomes enhanced.

In fact the 4 IRDC clumps we selected were found to have the highest levels of deuteration, $D_{\text{frac}} \equiv N_{\text{N}_2\text{D}^+}/N_{\text{N}_2\text{H}^+}$ among the 10 massive starless clouds studied by Fontani et al. (2011), with $D_{\text{frac}} = 0.38, 0.43, 0.40, 0.70$ for C1, F1, F2, G2, respectively. This compares with a mean $D_{\text{frac}} = 0.12$ for the other 6 sources in the sample, which were not selected from MIR extinction. This indicates that the MIREX-based selection method is efficient at finding regions that are cold and dense, and not yet forming stars. Note that the protostellar sources in the sample of Fontani et al. tend to have significantly lower values of $D_{\text{frac}} \simeq 0.04$, which is expected due to the warming of the infall envelope by the protostar.

Deuterated molecules have been shown to be the best kinematic probes of the coldest and densest conditions associated with low-mass star formation (e.g. Caselli et al. 2002; Crapsi et al. 2007). We will apply the same methods in the more extreme environments of IRDCs, where there tends to be a larger and more pressurized mass of cold, dense gas, compared to low-mass star-forming regions such as Taurus. We will thus use N_2D^+ to both identify pre-stellar cores — efficiently distinguishing them from their surrounding clump material — and then as their kinematic tracer.

1.3. Predictions of the Turbulent Core Accretion Model of Virialized Cores

MT03 modeled clumps and massive pre-stellar cores as singular polytropic virialized spheres in hydrostatic equilibrium, with power law density, $\rho \propto r^{-k_\rho}$, and pressure, $P \propto r^{-k_P}$, distributions with fiducial value $k_\rho = 1.5$ (for both clumps and cores), implying $k_P = 2(k_\rho - 1) = 1.0$. Such values are consistent with those derived from MIREX mapping by BT12, who found $k_{\rho,\text{cl}} \simeq 1.1$ (for clumps) and $k_{\rho,c} \simeq 1.6$ (for cores). MT03 assumed cores have a boundary with surface pressure, $P_{s,c}$, that is in approximate equilibrium with the pressure of the immediately surrounding environment of the star-forming clump. This pressure was assumed to be related to the mean pressure in the clump, \bar{P}_{cl} , via $P_{s,c} = \phi_{P,c} \bar{P}_{\text{cl}}$, where $\phi_{P,c}$ is a constant of order unity. The value of $\phi_{P,c}$ depends on the location of the core within the clump: MT03

TABLE 1
IRDC CORE/CLUMPS OBSERVING TARGETS

Core name ^a	RA(J2000) (h m s)	Dec(J2000) ($^{\circ}$ ' ")	$V_{\text{LSR}}^{\text{b}}$ (km s^{-1})	d^{c} (kpc)	$D_{\text{frac}}^{\text{b}}$
G028-C1	18:42:46.9	-04:04:08	+78.3	5.0	0.38
G034-F1 ^d	18:53:16.5	+01:26:10	+57.7	3.7 ^e	0.40
G034-F2 ^d	18:53:19.1	+01:26:53	+57.7	3.7 ^e	0.43
G034-G2	18:56:50.0	+01:23:08	+43.6	2.9	0.70

^aFrom BT12

^bFrom Fontani et al. (2011)

^cKinematic distance from Simon et al. (2006)

^dThe labeling of F1 and F2 was mistakenly interchanged in Fontani et al. (2011).

^eKurayama et al. (2011) report a parallax distance of 1.56 kpc for IRDC F, although the reliability of this has been questioned by Foster et al. (2012).

assumed cores were typically at radial locations of $0.3R_{\text{cl}}$ so that $\phi_{P,c} \simeq 2$ (for $k_{\rho,\text{cl}} = 1.5$). In this paper we will define the clump properties from the material that is more localized around each core: we set $R_{\text{cl}} = 2R_c$ and evaluate its mass surface density, Σ_{cl} , as the average value (observed via the MIREX maps) in the annulus from R_c to $2R_c$. In this case, $\phi_{P,c} = (1 - k_P/3)(R_c/R_{\text{cl}})^{-k_P} \rightarrow 4/3$ in the fiducial case of $k_\rho = 1.5, k_P = 1$ (and 1.07 in the case of $k_\rho = 1.1, k_P = 0.2$).

MT03 assumed the mean pressure in the clump was set by its self-gravitating weight, i.e. $\bar{P}_{\text{cl}} \equiv \phi_{\bar{P}} G \Sigma_{\text{cl}}^2$, where $\phi_{\bar{P}} = (3\pi/20) f_g \phi_{\text{geom}} \phi_B \alpha_{\text{vir,cl}}$, where f_g is the gas mass fraction of the clump, ϕ_{geom} is a numerical factor of order unity that accounts for the effect of nonspherical geometry, ϕ_B accounts for the effect of magnetic fields and $\alpha_{\text{vir,cl}} \equiv 5(\sigma_{\text{cl}}^2) R_{\text{cl}} / (GM_{\text{cl}})$ is the virial parameter of the clump. MT03 adopted a fiducial value of $f_g = 2/3$ (with the remainder composed of a nascent stellar cluster), but for the IRDC clumps we consider here, we will assume $f_g = 1$. Aspect ratios of up to 2:1 (i.e., eccentricity of a projected elliptical shape $e \leq 0.87$) lead to $\phi_{\text{geom}} \lesssim 1.1$, so such elongations are a relatively minor effect and, like MT03, we assume $\phi_{\text{geom}} = 1$. For magnetic field strengths such that the Alfvén Mach number $m_A \equiv \sqrt{3}\sigma/v_A = 1$, where $v_A = B/\sqrt{4\pi\rho}$ is the Alfvén speed, MT03 showed that $\phi_B = 1.3 + 1.5m_A^{-2} \rightarrow 2.8$. Below, for our fiducial estimates, we will consider the possibility of a range $0.5 < m_A < 2$, corresponding to $7.3 > \phi_B > 1.7$. Finally, we assume that the clump is virialized with $\alpha_{\text{vir,cl}} = 1$. With these values $\phi_{\bar{P}} = 1.32$ (c.f. 0.88 in MT03).

The radius of a core in virial equilibrium, including pressure equilibrium with its surroundings, is (MT03)

$$R_{\text{c,vir}} = 0.071 \left(\frac{A}{k_P^2 \phi_{P,c} \phi_{\bar{P}}} \right)^{1/4} \left(\frac{M_c}{60 M_\odot} \right)^{1/2} \left(\frac{\Sigma_{\text{cl}}}{1 \text{ g cm}^{-2}} \right)^{-1/2} \text{ pc} \quad (1)$$

$$R_{\text{c,vir}} \rightarrow 0.0574 \left(\frac{M_c}{60 M_\odot} \right)^{1/2} \left(\frac{\Sigma_{\text{cl}}}{1 \text{ g cm}^{-2}} \right)^{-1/2} \text{ pc}, \quad (2)$$

where $A = (3 - k_\rho)(k_\rho - 1)f_g \rightarrow 3/4$. The mass average velocity dispersion of a virialized core is related to that at the surface via $\sigma_{\text{c,vir}} = [2(3 - k_\rho)/(8 - 3k_\rho)]\sigma_{\text{c,s}} \rightarrow (6/7)\sigma_{\text{c,s}}$. Note that $\sigma_c = c_c/\phi_B^{1/2}$, where $c_c \equiv (P_c/\rho_c)^{1/2}$ is the effective sound speed in the core, so that

$$\sigma_{\text{c,vir}} = 1.91 \frac{2(3 - k_\rho)}{8 - 3k_\rho} \left(\frac{\phi_{P,c} \phi_{\bar{P}}}{A k_P^2 \phi_B^4} \right)^{1/8} \left(\frac{M_c}{60 M_\odot} \right)^{1/4} \left(\frac{\Sigma_{\text{cl}}}{1 \text{ g cm}^{-2}} \right)^{1/4} \text{ km s}^{-1} \quad (3)$$

$$\sigma_{\text{c,vir}} \rightarrow 1.09 \left(\frac{M_c}{60 M_\odot} \right)^{1/4} \left(\frac{\Sigma_{\text{cl}}}{1 \text{ g cm}^{-2}} \right)^{1/4} \text{ km s}^{-1}. \quad (4)$$

The above expressions can also be combined to give a velocity dispersion (or FWHM line width, $\Delta v_{\text{vir}} = (8\ln 2)^{1/2} \sigma_{\text{vir}} = 2.355\sigma_{\text{vir}}$) versus size relation:

$$\sigma_{\text{c,vir}} = 2.27 \frac{2(3 - k_\rho)}{8 - 3k_\rho} \left(\frac{\phi_{P,c} \phi_{\bar{P}}}{A \phi_B^2} \right)^{1/4} \left(\frac{\Sigma_{\text{cl}}}{1 \text{ g cm}^{-2}} \right)^{1/2} \left(\frac{R_{\text{c,vir}}}{0.1 \text{ pc}} \right)^{1/2} \text{ km s}^{-1} \quad (5)$$

$$\sigma_{\text{c,vir}} \rightarrow 1.44 \left(\frac{\Sigma_{\text{cl}}}{1 \text{ g cm}^{-2}} \right)^{1/2} \left(\frac{R_{\text{c,vir}}}{0.1 \text{ pc}} \right)^{1/2} \text{ km s}^{-1}. \quad (6)$$

We will now compare these predictions, in particular for $\sigma_{\text{c,vir}}$ and $R_{\text{c,vir}}$, with our sample of massive starless cores.

2. OBSERVATIONS

We used ALMA in Cycle 0 compact configuration to observe $\text{N}_2\text{D}^+(3-2)$ (231 GHz, Band 6, $\simeq 2.3''$ angular resolution, $\sim 9''$ maximum detectable scale, $27''$ field of view, 0.08 km s^{-1} velocity resolution) with a single pointing for each core, centered at the peak Σ of the BT12 MIREX map, and sharing one track amongst the 4 sources with a total integration time of about 1.0 hour per source. Several other species, $\text{DCO}^+(3-2)$, $\text{DCN}(3-2)$, $^{13}\text{CS}(5-4)$ and $\text{SiO}(5-4)$ were also searched for in the same spectral setup. We achieved 1σ RMS noise levels of about 11 and 7.0 mJy/beam per 0.08 km/s channel for $\text{N}_2\text{D}^+(3-2)$ (231.32186 GHz) and $\text{DCO}^+(3-2)$ (216.11258 GHz), respectively.

From the line-free regions of the four spectral windows we measured the continuum flux with an average wavelength of 1.338 mm . The values of the 1σ RMS noise per beam in C1, F1, F2, G2 were 0.272, 0.213, 0.336, 0.174 mJy/beam , respectively.

3. RESULTS

3.1. Identification of starless cores via N_2D^+ emission

The integrated intensity maps of $\text{N}_2\text{D}^+(3-2)$ and $\text{DCO}^+(3-2)$ of the clumps C1, F1, F2, G2 are shown in Fig. 1b & c as contour plots overlaid on top of the MIREX Σ maps. Strong detections of both lines are seen in all cases. $\text{DCN}(3-2)$, $^{13}\text{CS}(5-4)$ and $\text{SiO}(5-4)$ were not detected, even from stacked rest-frame spectra towards the N_2D^+ cores. Continuum emission from the line-free regions of the four spectral windows, with mean wavelength of 1.338 mm , was detected and is shown in Fig. 1d.

The critical density of $\text{N}_2\text{D}^+(3-2)$ is $2.9 \times 10^6 \text{ cm}^{-3}$, while that of $\text{DCO}^+(3-2)$ is $3.5 \times 10^6 \text{ cm}^{-3}$. However, the emission from DCO^+ tends to be more widespread. We expect this is because DCO^+ (formed via $\text{CO} + \text{H}_2\text{D}^+$) is following the more extended distribution of CO, which is likely to suffer significant depletion in the cold, high-density cores, where

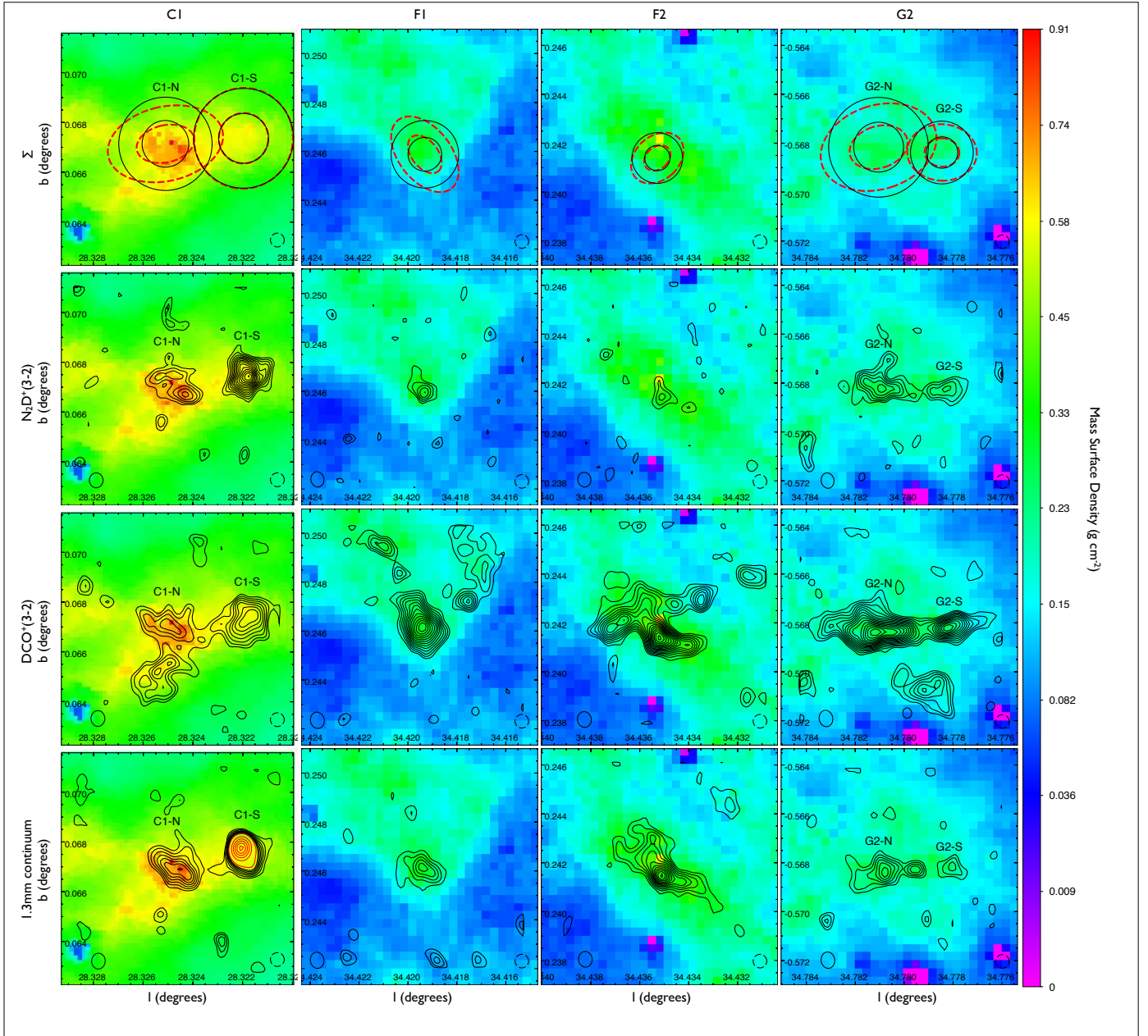


FIG. 1.— The four massive starless core/clumps observed by ALMA: columns from left to right show C1, F1, F2, G2. The background colors in all rows show MIREX Σ maps in g cm^{-2} (Butler, Tan & Kainulainen 2013 for C1; BT12 for F1, F2 and G2). The *Spitzer*-IRAC $2''$ beam is shown in the lower right of the panels. (a) *First row*: Analytic regions used to define the cores and their surrounding clump environments. The inner ellipses and equivalent area circles show the deconvolved extent of the N_2D^+ cores identified in row (b), while the outer ellipses and circles have a radius twice as large and define the annuli used to estimate the surrounding clump envelope. (b) *Second row*: ALMA Cycle 0 observations of $\text{N}_2\text{D}^+(3-2)$ integrated intensity, contours shown from $2, 3, 4, \dots, \sigma$. Six cores, C1-N, C1-S, F1, F2, G2-N & G2-S, are defined by their 3σ contours in position-velocity space. The ALMA beam is shown in the lower left of each panel. Note that not all high Σ regions show strong N_2D^+ emission, but N_2D^+ cores do correlate well with structures seen in the MIREX maps. (c) *Third row*: ALMA observations of $\text{DCO}^+(3-2)$ integrated intensity, contours shown from $2, 3, 4, \dots, \sigma$, which is generally more widespread than N_2D^+ . (d) *Fourth row*: ALMA observations of the 1.34 mm dust continuum emission, with contours from $2, 3, 4, \dots, 8\sigma$ (black) then (for C1) $10, 20, 30, \dots, 60\sigma$ (red).

N_2D^+ is enhanced. There is generally good correspondence between the morphology of the line emission and structures seen in the MIREX maps. For example, the “V”-shaped structure of DCO^+ emission in F1 is also seen in the MIREX map. Even quite weak DCO^+ features, e.g. in G2, can show themselves via MIR extinction.

Some, but not all, localized MIREX column density structures reveal themselves via $\text{N}_2\text{D}^+(3-2)$. Following the results of studies of low-mass starless cores described in §1, we define these to be starless core candidates, finding 6 objects (C1-N, C1-S, F1, F2, G2-N & G2-S) that have emission exceeding the 3σ noise level within $l - b - v$ -space. Positional core boundaries are defined using the projection of this 3σ contour, after deconvolving with a Gaussian equivalent to the

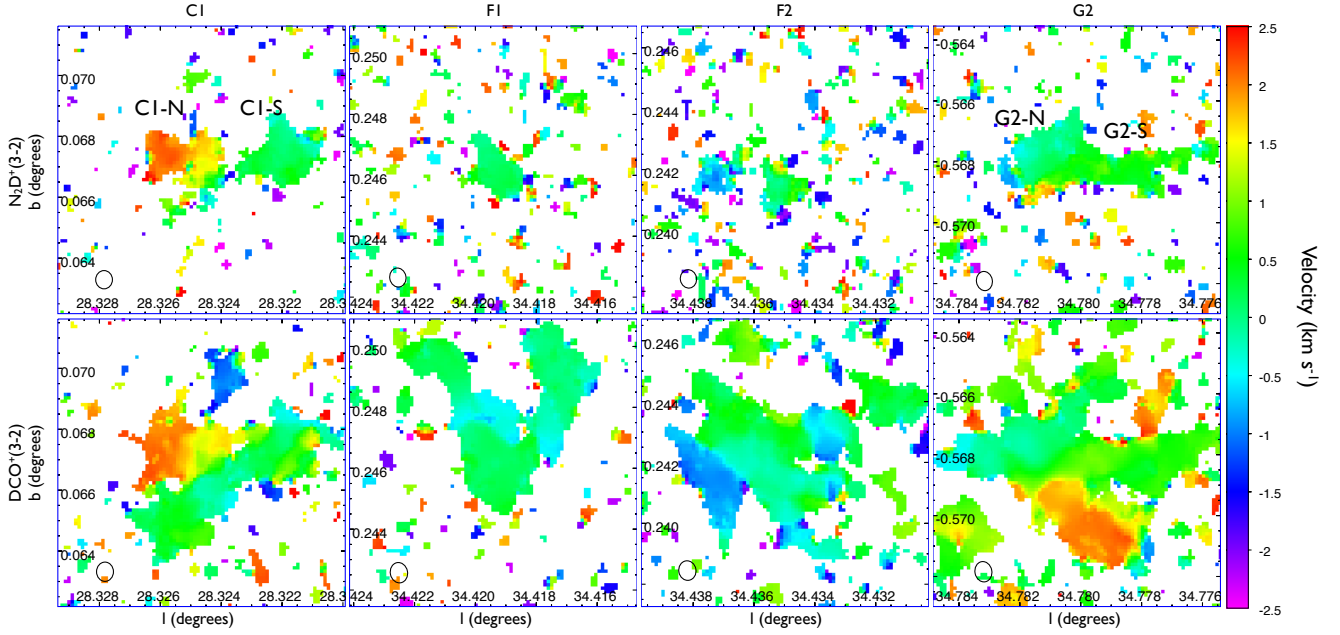


FIG. 2.— First moment (mean velocity) maps of the four core/clumps: columns from left to right show C1, F1, F2, G2. (a) *First row:* First moment map of $\text{N}_2\text{D}^+(3-2)$ emission, integrated over a 5 km/s velocity range centered on the mean N_2D^+ core velocities of C1-S, F1, F2 and G2-N. The ALMA beam is shown in the lower left of each panel. Only regions that have some contribution from cells with intensities $\geq 3\sigma$ are displayed in color. (b) *Second row:* First moment map of $\text{DCO}^+(3-2)$ emission in the same velocity reference frames as in row (a).

ALMA synthesized beam. The positions, elliptical eccentricities and position angles, and equivalent area radial sizes, R_c , are listed in Table 2. The diameters of the cores are all larger than the angular resolution of the observations. Core C1-N appears to exhibit some substructure in its $\text{N}_2\text{D}^+(3-2)$ emission, whereas the other sources appear to be relatively monolithic.

The morphology of the continuum emission also generally matches that seen in the molecular line emission, especially that traced by $\text{N}_2\text{D}^+(3-2)$.

3.2. Core kinematics and velocity dispersion

In Fig. 2 we show the first moment maps of the 4 core/clumps as traced by $\text{N}_2\text{D}^+(3-2)$ and $\text{DCO}^+(3-2)$. We only include the contribution from cells in the position-velocity cube that have a signal more than 3σ above the noise in each 0.08 km/s channel. We integrate over a velocity range of $\pm 2.5 \text{ km s}^{-1}$ centered on the mean velocity of the N_2D^+ cores C1-S, F1, F2, and G2-S (evaluated below). In the C1 region, cores C1-N and S show a velocity offset of 1.8 km s^{-1} , but with some N_2D^+ emission at intermediate velocities (we checked that all significant emission associated with C1-N is captured by the velocity interval used in Fig. 2). In G2, the cores are within 0.4 km s^{-1} of each other. On the larger scales of the $\text{DCO}^+(3-2)$ emission the first moment maps generally reveal quite disordered structure, with multiple discrete features spanning a velocity range of a few km s^{-1} . The exception is F1, which shows quite coherent velocity structure across its “V”-shaped morphology.

In Fig. 3 we show the second moment (velocity dispersion) maps of the four core/clumps. To evaluate these, only regions that have at least one cell in the velocity range used for the first moment map with intensity $\geq 5\sigma$ are considered. Then the velocity dispersion is evaluated from those cells that have signal $\geq 3\sigma$. This truncation will tend to lead to an underestimation of the true dispersion, especially for regions with weak signal (below, when we evaluate the velocity dispersion of cores with defined areas, we will do so by fitting directly to the total spectrum). For the $\text{N}_2\text{D}^+(3-2)$ emission we also subtract off in quadrature the contribution to line broadening, 0.242 km s^{-1} , from the main group of hyperfine lines (over a velocity range of $\pm 1 \text{ km s}^{-1}$ about the peak line). This assumes the lines are optically thin, which is consistent with our analysis of core spectra (below). This hyperfine broadening can be larger than the observed velocity dispersion in regions with relatively low signal to noise ratios, and in this case we set the map at this location to have an unmeasured value. In order to have sufficient signal to noise to see extended structure in the velocity dispersion maps of some of the cores, we smoothed the N_2D^+ map with a $3''$ beam.

Fig. 3 reveals velocity dispersions that are typically a fraction of a km s^{-1} . Low velocity dispersion halos around some structures are likely caused by the signal to noise ratio threshold, described above, that is used to select regions in position-velocity space for analysis. Nevertheless, real structure can be seen in the maps, especially those of DCO^+ . Structures showing larger velocity dispersion can be real, e.g. as the result of local virialized motions in a core or clump, or can result from overlapping independent components. A more detailed comparison of the observed velocity structures with the results of numerical simulations of molecular clouds will be carried out in a future paper.

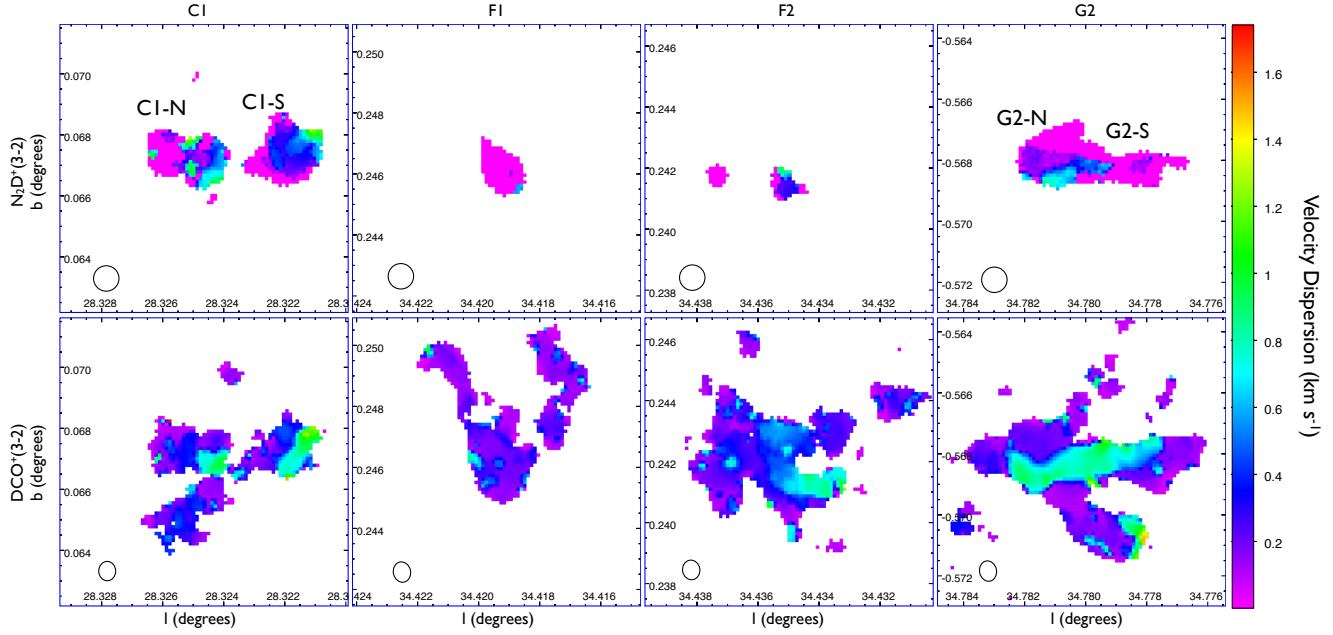


FIG. 3.— Second moment (velocity dispersion $\sigma_{\text{N}_2\text{D}^+, \text{obs}}$ and $\sigma_{\text{DCO}^+, \text{obs}}$) maps of the four core/clumps: columns from left to right show C1, F1, F2, G2. (a) *First row*: Second moment map of $\text{N}_2\text{D}^+(3-2)$ emission, smoothed with a $3''$ beam, integrated over a 5 km/s velocity range centered on the mean N_2D^+ core velocities of C1-S, F1, F2 and G2-S. Only regions meeting signal to noise threshold requirements to measure velocity dispersion (see text) are displayed in color. (b) *Second row*: Second moment map of $\text{DCO}^+(3-2)$ emission (unsmoothed) in the same velocity reference frames as in row (a).

We now focus on the velocity dispersion of the identified N_2D^+ cores. The integrated $\text{N}_2\text{D}^+(3-2)$ spectra of the cores identified in §3.1 are shown in Fig. 4. We fit model spectra, which account for the full blended set of 47 hyperfine components, to these data to derive the centroid velocity, $V_{\text{LSR}, \text{N}_2\text{D}^+}$, and the observed 1D velocity dispersion, $\sigma_{\text{N}_2\text{D}^+, \text{obs}}$, also listed in Table 2. This modeling allows for the possibility of optically thick parts of the hyperfine line complex, but we find all spectra can be well-modeled assuming optically thin line emission. Note, these values for the cores can appear larger than those displayed in Fig. 3, since the former includes the contribution from large-scale gradients in centroid velocity across the core. We assume a gas temperature of $T = 10 \pm 3 \text{ K}$ (see § 3.3.2) to remove the thermal component of the line to thus assess the nonthermal component of the velocity dispersion. We then sum this in quadrature with the sound speed of the molecular cloud, assuming the same temperature value of $10 \pm 3 \text{ K}$ and a mean particle mass of $\mu = 2.33m_p$, to derive the total core velocity dispersion as derived from $\text{N}_2\text{D}^+(3-2)$ emission, $\sigma_{\text{N}_2\text{D}^+}$.

We do not use DCO^+ to measure core kinematics since it is expected to be somewhat under abundant in CO-depleted regions and thus likely to preferentially trace the extended core envelopes. Nevertheless we present in Table 2 the values of $V_{\text{LSR}, \text{DCO}^+}$ and $\sigma_{\text{DCO}^+, \text{obs}}$, integrated over the same region of the N_2D^+ -defined core. The centroid velocities of $\text{N}_2\text{D}^+(3-2)$ and $\text{DCO}^+(3-2)$ are very similar (always within 0.2 km s^{-1}), while the observed velocity dispersion of DCO^+ tends to be larger by up to $\sim 35\%$, which is probably related to this species tracing a larger region around the core.

3.3. Core and clump mass surface density, mass and density estimates

3.3.1. Estimates from MIREX maps

We use the BT12 MIREX maps to estimate the mass surface density of the clump material, Σ_{cl} , immediately surrounding the identified cores, from annuli extending from R_c to $2R_c$. This choice of size of the annulus follows the method of BT12 (see also §1.3). We have investigated apertures based on the elliptical shapes derived from the N_2D^+ emission that define the cores and based on equivalent area circles. The resulting differences in the derived quantities are typically very minor, $\lesssim 10\%$, so for simplicity we only report results based on equivalent area circular apertures.

We find values of $\Sigma_{\text{cl}} \simeq 0.2 - 0.3 \text{ g cm}^{-2}$ (Table 2). We assume these estimates have a 30% uncertainty due to the choice of opacity per unit gas mass in the IRDC material (BT12 assume $\kappa_{8\mu\text{m}} = 7.5 \text{ cm}^2 \text{ g}^{-1}$ based on the moderately coagulated thin ice mantle model of Ossenkopf & Henning 1994). However, in very high column density regions, the MIREX method of BT12 will begin to underestimate the true value of Σ , when the background intensity that makes it through the cloud becomes comparable to the instrumental noise in the image. BT12 refer to these as “saturated” regions. Only F2 is formally classified as “saturated” by BT12, but this is based on a global definition within the IRDC and does not allow for modest variations in the foreground intensity across the cloud.

Butler, Tan & Kainulainen (2013) (BTK) have examined archival *Spitzer*-IRAC data on IRDC C that probe to significantly smaller instrumental noise levels than the *Spitzer*-GLIMPSE images analyzed by BT12. We have evaluated Σ_{cl} from these BTK maps and find values that are 54% and 53% larger for C1-S and C1-N, respectively. We will perform

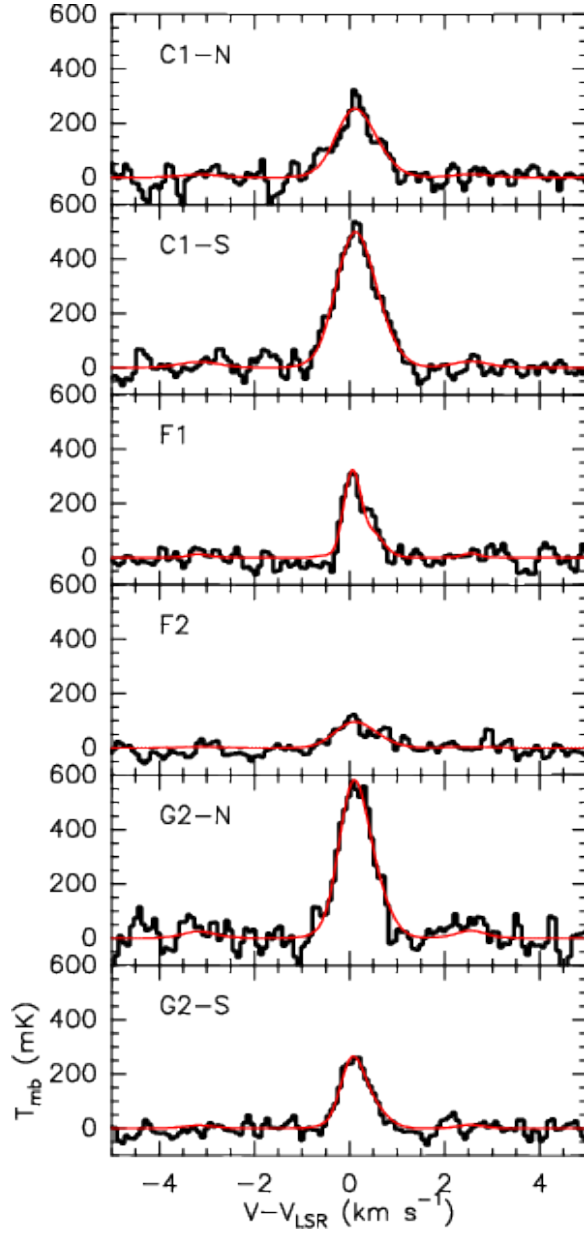


FIG. 4.— $\text{N}_2\text{D}^+(3-2)$ spectra (V_{LSR} -frame) of the six identified cores: C1-N, C1-S, F1, F2, G2-N & G2-S, shown at the maximum resolution of 0.08 km s^{-1} . The red continuous line shows the best fit model profiles.

our dynamical analysis for the following cases: (1) uniformly using the BT12 maps for all 6 cores; (2) replacing the BT12 maps with the BTK maps for cores C1-S and C1-N (these entries are shown in square brackets in Table 2).

We then use the MIREX maps to evaluate the maximum mass surface density of the core, $\Sigma_{c,\text{max}}$, averaged inside R_c . In one sense this is an upper limit for the core properties because it assumes all the line of sight material in the IRDC is associated with the core. However, because of potential saturation in the MIREX maps, our estimates of the total mass surface density through the IRDCs in these regions could be underestimates. From the BT12 maps, we find $\Sigma_{c,\text{max}} \simeq 0.2 - 0.4 \text{ g cm}^{-2}$, only slightly higher than the values of Σ_{cl} . This suggests that either only a small fraction of the total column of material along the line of sight is associated with the core (with the rest being part of the surrounding clump) or that the mass surface densities of the cores are underestimated because of saturation in the MIREX maps. To assess this latter possibility, for the C1 cores we also evaluate $\Sigma_{c,\text{max}}$ from the BTK map, finding values that are 65% and 58% larger for C1-S and C1-N, respectively, than those derived from the BT12 maps. In the BTK map, these cores have values of $\Sigma_{c,\text{max}}$ that are both 16% larger than Σ_{cl} (compared to 8.5% and 13% for C1-S and C1-N, respectively, in the BT12 maps). As a result of the uncertainty in assessing what fraction of $\Sigma_{c,\text{max}}$ is associated with the cores, after first deriving core properties based simply on $\Sigma_{c,\text{max}}$, we will also consider two further methods to estimate Σ_c .

Utilizing $\Sigma_{c,\text{max}}$, the “maximum” core mass is derived as $M_{c,\text{max}} = \Sigma_{c,\text{max}} \pi R_c^2$. We assume 20% distance uncertainties (we have adopted the kinematic distance estimates of Simon et al. 2006), which leads to 50% total uncertainties in $M_{c,\text{max}}$

(summing errors in quadrature). However, IRDC F has a reported astrometric distance of 1.56 kpc (Kurayama et al. 2011), only 42% of the kinematic distance. We thus perform a separate analysis for the F cores using this closer distance (these entries are shown in rounded brackets in Table 2). Note however that Foster et al. (2012) have called into question the validity of the astrometric distance, since the data quality on which it is based are relatively poor and the implied streaming motions if it is correct are very large ($\sim 30 \text{ km s}^{-1}$).

The derived maximum core masses, $M_{c,\text{max}}$, are in the range from ~ 1 to $\sim 60 M_{\odot}$. C1-N & S have similar masses at the upper end of this range (using the BTK maps) and have the potential to form massive (i.e. $> 8 M_{\odot}$) stars. Next, G2-N has about $9 M_{\odot}$, followed by the F cores (assuming the kinematic distance) and then G2-S. These may be the progenitors of intermediate-mass or even low-mass stars. Note, however, that these star-forming environments are at significantly higher mass surface densities, and thus pressures, than most previously studied regions of low-mass star formation, such as in the Taurus molecular cloud.

With $\Sigma_{c,\text{max}}$ and R_c we can also estimate the maximum volume density assuming spherical geometry. Table 2 lists values of the maximum total H nuclei number density as $n_{\text{H},c,\text{max}} = 3M_{c,\text{max}}/(4\pi R_c^3 \mu_{\text{H}})$, which given the above assumptions have 36% uncertainties. These values range from a few $\times 10^5 \text{ cm}^{-3}$ to few $\times 10^6 \text{ cm}^{-3}$.

We now attempt to account for the overlying clump material that is not associated with the cores. First, we assume this material has the same column density as the surrounding clump evaluated from R_c to $2R_c$. We expect that subtracting off this clump envelope leads to a minimum estimate of the core mass, since if the local IRDC geometry is sheet-like or filamentary this would lead to an overestimate of the clump material that is along the line of sight to the core. We evaluate $\Sigma_{c,\text{min}} = \Sigma_{c,\text{tot}} - \Sigma_{\text{cl}}$ and list its values in Table 2. We also then derive $M_{c,\text{min}}$ and $n_{\text{H},c,\text{min}}$. This method of envelope subtraction substantially reduces the estimated core mass by factors of about five to ten. The most massive cores, C1-S & N now have masses of about $10 M_{\odot}$ (using the BTK maps). By this method, the estimated densities are now $\lesssim 10^5 \text{ cm}^{-3}$.

3.3.2. Estimates from 1.34 mm dust continuum emission

Additionally, we utilize the observed 1.338 mm continuum emission to estimate core properties. Our ALMA Cycle 0 compact configuration observations are sensitive to angular scales from $\sim 2''$ to $9''$, so will tend to pick out core rather than clump material. The total mass surface density corresponding to a given specific intensity of mm continuum emission is

$$\Sigma_{\text{mm}} = 6.03 \times 10^{-3} \left(\frac{S_{\nu}/\Omega}{\text{MJy/sr}} \right) \left(\frac{\kappa_{\nu}}{0.01 \text{ cm}^2 \text{ g}^{-1}} \right)^{-1} \lambda_{1.338}^3 \left[\exp \left(1.075 T_{d,10}^{-1} \lambda_{1.338}^{-1} \right) - 1 \right] \text{ g cm}^{-2}, \quad (7)$$

where $\lambda_{1.338} = \lambda/1.338 \text{ mm}$ and $T_{d,10} = T_d/10 \text{ K}$. At this frequency, our preferred choice of $\kappa_{\nu} = 5.95 \times 10^{-3} \text{ cm}^2 \text{ g}^{-1}$, based on the moderately coagulated thin ice mantle dust model of OH94 and assuming a total (gas plus dust)-to-refractory-component-dust-mass ratio of 141 (Draine 2011). OH94 dust models that are more coagulated have κ_{ν} that is about 23% larger. Overall we adopt a 30% uncertainty in κ_{ν} .

An estimate of the dust temperature is also needed. From observations of ammonia inversion transitions, Pillai et al. (2006) measured IRDC temperatures $\sim 15 \text{ K}$. However, we expect such observations tend to probe the lower density envelopes around the IRDC cores, as the inversion transitions of NH_3 have critical densities of only $\sim 10^4 \text{ cm}^{-3}$. The dust temperature can also be constrained from the FIR spectral energy distribution. For example, fitting *Herschel* PACS and SPIRE data, Peretto et al. (2010) found temperatures of $\sim 10 - 12 \text{ K}$ in the central region of an IRDC.

Here we use the fact that some IRDC cores are seen in absorption at wavelengths as long as $\sim 100 \mu\text{m}$ to place constraints on the dust temperature. This method has the advantage of allowing us to derive constraints on scales of the *Herschel* angular resolution, i.e. down to $6''$ for the $70 \mu\text{m}$ band. Approximating the cloud as a 1D slab that has a total optical depth τ_{ν} at frequency ν and integrating the radiative transfer equation yields

$$I_{\nu,1} = I_{\nu,0} e^{-\tau_{\nu}} + \int_0^{\tau_{\nu}} e^{-(\tau_{\nu}-\tau'_{\nu})} (j_{\nu}/\kappa_{\nu}) d\tau'_{\nu}, \quad (8)$$

where $I_{\nu,1}$ is the transmitted intensity towards the observer from the near side of the cloud, $I_{\nu,0}$ is the background incident intensity on the far side of the cloud, j_{ν} is the emissivity of the cloud material (i.e. its dust), and κ_{ν} is the cloud opacity. Approximating the dust in the IRDC as being in thermal equilibrium and at a constant temperature so that $j_{\nu}/\kappa_{\nu} \rightarrow B_{\nu}(T_d) \equiv (2h\nu^3/c^2)(e^{h\nu/kT_d} - 1)^{-1}$, the Planck function, we have

$$\frac{I_{\nu,1}}{I_{\nu,0}} = e^{-\tau_{\nu}} + \frac{B_{\nu}(T_d)}{I_{\nu,0}} (1 - e^{-\tau_{\nu}}). \quad (9)$$

The background intensity can be estimated empirically from the observed emission in the Galactic plane. Li & Draine (2001) considered Galactic infrared emission in the MIRS region ($44^{\circ} \leq l \leq 44^{\circ}40'$, $-0^{\circ}40' \leq b \leq 0^{\circ}$). Integrating their model over the *Herschel*-PACS bands at 70, 100, 160 μm gives intensities $I_{\nu} = 500, 1270, 1690 \text{ MJy sr}^{-1}$ at mean wavelengths of 74.0, 103.6, 161.6 μm , respectively. At $l = 30^{\circ}, b = 0^{\circ}$, Bernard et al. (2010) estimated ‘‘offset’’ intensities of 688.0 and 1982.3 MJy sr^{-1} for the PACS 70 and 160 μm bands, which provides an approximate estimate for the intensity of the diffuse emission in this direction. Using an average scaling factor of 1.27, the 100 μm flux at $l = 30^{\circ}$ is estimated to be 1620 MJy sr^{-1} . Our target IRDCs C, F, G are at $l = 28.3^{\circ}, 34.4^{\circ}, 34.8^{\circ}$, so we will use the results for $l = 30^{\circ}$. BT09 estimated that for IRDCs C, F, G the fraction of diffuse emission that is in the foreground of the

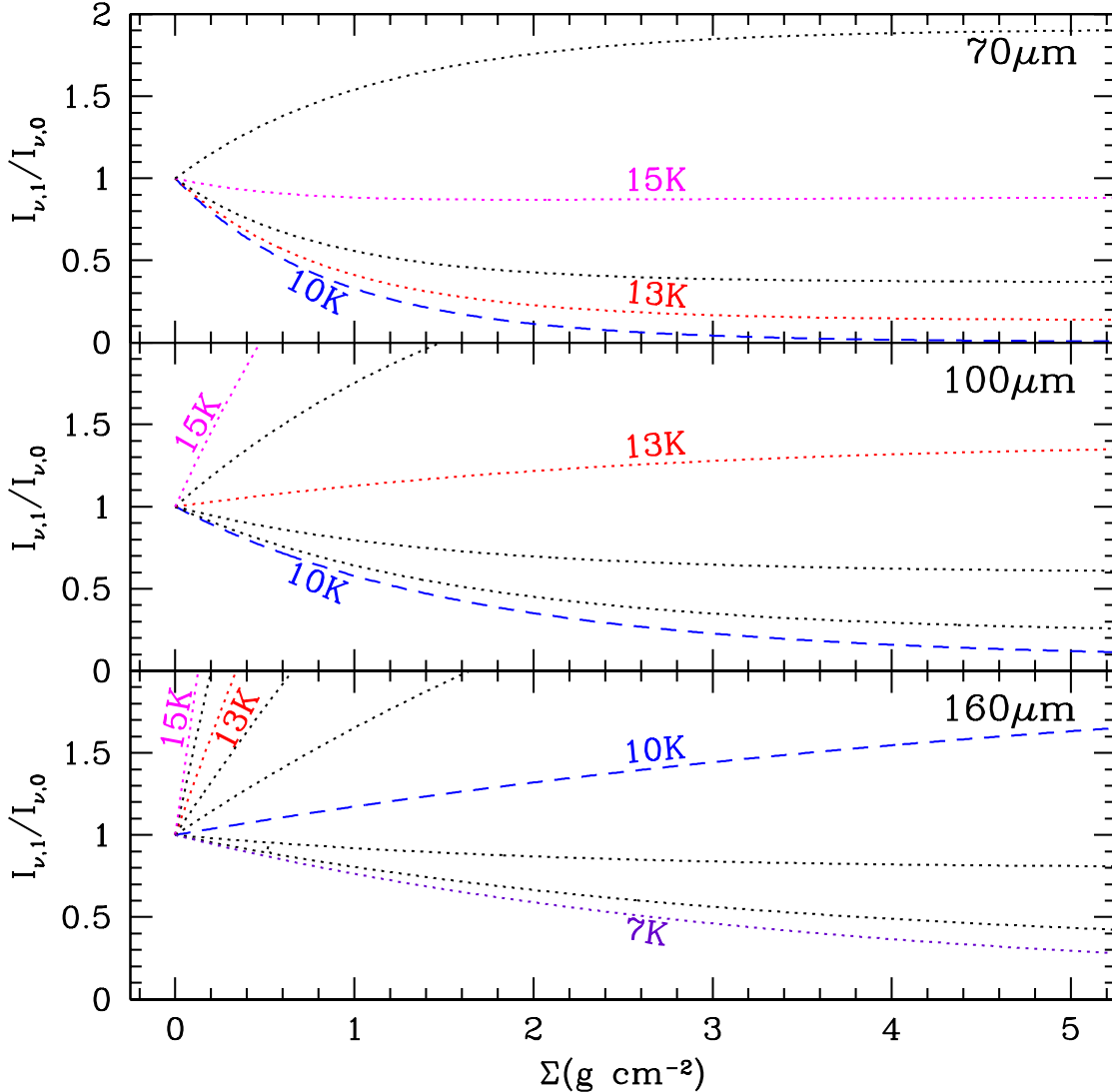


FIG. 5.— Dependence of $I_{\nu,1}/I_{\nu,0}$ with Σ in the *Herschel*-PACS 70, 100, & 160 μm wavebands for IRDCs near $l = 30^\circ$ and for various dust temperatures (the dotted lines show 1K increments between the labeled temperatures). OH94 moderately coagulated thin ice mantle dust opacities have been adopted. Note the cloud needs to be cold ($\lesssim 15, 12, 9$ K) to appear dark at 70, 100, 160 μm , respectively.

cloud is 0.266, 0.193, 0.14, respectively. Adopting a value of 0.2, so that 80% of the observed intensity is the value of the background intensity behind the IRDCs, we have $I_{\nu,0} = 550, 1290, 1590$ MJy sr^{-1} .

With the above fiducial values of $I_{\nu,0}$, Figure 5 shows $I_{\nu,1}/I_{\nu,0}$ as a function of mass surface density, $\Sigma = \tau_\nu/\kappa_\nu$, for different dust temperatures, T_d . We have evaluated $I_{\nu,1}/I_{\nu,0}$ for the fluxes that would be received in the 70, 100, 160 μm , i.e. the *Herschel*-PACS wavebands, integrating over the filter response function, the Li & Draine (2001) spectrum of the diffuse Galactic background emission, and over the OH94 opacity function (we find mean opacities of $\kappa_{70\mu\text{m}} = 1.14 \text{cm}^2 \text{g}^{-1}$, $\kappa_{100\mu\text{m}} = 0.603 \text{cm}^2 \text{g}^{-1}$ and $\kappa_{160\mu\text{m}} = 0.290 \text{cm}^2 \text{g}^{-1}$ for the OH94 moderately coagulated thin ice mantle dust model).

We examined images of the IRDCs in the *Herschel* data archive. IRDC C has been imaged at 70, 100 & 160 μm . At 70 μm , C1 appears globally dark (i.e. relative to the low-intensity diffuse emission beyond the BT09 ellipse, not just locally dark with respect to its immediate surroundings). At 100 μm it has a similar, perhaps slightly lower, intensity as the faintest parts of the IRDC surroundings, while at 160 μm it appears moderately brighter (although is still locally dark). Comparison with Fig. 5 suggests a (mass-weighted line of sight) temperature of $\simeq 10$ K at C1. IRDC F has images at 70 & 160 μm . F1 & F2 are locally dark at 70 μm . While F2 also appears to be globally dark, this does not appear to be the case for F1 due to the relative proximity of bright sources. At 160 μm , the intensities towards both F1 & F2 are brighter than the diffuse surroundings. IRDC G has images at 70 & 160 μm . G2 appears globally dark at 70 μm , but brighter than the IRDC surroundings at 160 μm .

Note that we expect the temperature in the N_2D^+ cores to be lower than the above constraints from ~ 100 μm shadowing, which are mass-weighted averages along the line of sight through the IRDC. Studies of lower-mass starless

cores have seen temperatures down to ~ 6 K in the very central regions (e.g. Crapsi et al. 2007; Pagani et al. 2009). Given the above constraints, we adopt a dust temperature of $T_d = 10 \pm 3$ K for the N_2D^+ cores. As we will see, the densities are high enough that we expect the gas and dust temperatures to be well-coupled, so we set $T = T_d$.

We then evaluate $\Sigma_{\text{c,mm}}$ via eq. 7. Since the uncertainties introduced by temperature are quite large and asymmetric, we show upper and lower uncertainty bounds separately (we have combined uncertainties in quadrature for the upper and lower sides separately). The values of $\Sigma_{\text{c,mm}}$ are always greater than $\Sigma_{\text{c,min}}$. They are less than $\Sigma_{\text{c,max}}$, except in the case of C1-S, where it is about 5% greater than the BTK $\Sigma_{\text{c,max}}$ value. These values still agree given the uncertainties.

We then proceed to derive masses ($M_{\text{c,mm}}$) and densities ($n_{\text{H,c,mm}}$) based on Σ_{mm} . We will tend to regard the core masses derived from mm dust emission as the most accurate measure, rather than $M_{\text{c,max}}$ or $M_{\text{c,min}}$. This is because the interferometric observations of the mm continuum emission filter out contributions from structures $\gtrsim 9''$, which are the scales expected of the surrounding clump. The cores themselves have diameters ranging from $3.7''$ to $7.3''$. Note, that $M_{\text{c,mm}}$ still has uncertainties of about a factor of 2, due to assumed temperature (± 3 K), opacity (30%) and distance (20%) uncertainties.

3.4. Dynamical state of the cores

For each estimate of core mass, i.e. $M_{\text{c,max}}$, $M_{\text{c,min}}$ and $M_{\text{c,mm}}$, we calculate $\sigma_{\text{c,vir}}$ from equation (4). In each case, we first consider the properties of the cores and their clump envelopes as derived from the BT12 MIREX maps. We also show the results for C1-N and S when using the BTK extinction map, and the results for F1 and F2 when adopting the near distance of 1.56 kpc (see Table 2). In addition to the uncertainties in $\sigma_{\text{c,vir}}$ due to errors in M_{c} and Σ_{cl} , we also allow for a range of magnetic field strengths in the core, such that $0.5 < m_A < 2$, i.e. $7.3 > \phi_B > 1.7$ (see §1.3). We then evaluate the ratio of the observed velocity dispersion derived from the $\text{N}_2\text{D}^+(3-2)$ spectrum to the prediction from virial equilibrium, $\sigma_{\text{N}_2\text{D}^+}/\sigma_{\text{c,vir}}$. We average these values for the sample of 6 cores (assuming the uncertainties are uncorrelated, although in reality there are likely to be correlated systematic uncertainties, e.g. affecting mass determinations due to choice of κ or T_d). We present three averages: first with core properties derived from the BT12 maps, second with the C1 cores evaluated using the BTK maps (and the remaining cores with the BT12 maps), and third being the same as the second case, but with the F cores evaluated at the near distance. We regard the second case as being the most accurate. We repeat the above analysis for $R_{\text{c,vir}}$ (evaluated from eq. 2) and the ratio $R_{\text{c}}/R_{\text{c,vir}}$ (note the distance uncertainty does not affect $R_{\text{c}}/R_{\text{c,vir}}$).

Quoting results for the second case, for $M_{\text{c,max}}$ the core sample has $\sigma_{\text{N}_2\text{D}^+}/\sigma_{\text{c,vir}} \simeq 0.659 \pm 0.085$, i.e. moderately sub-virial, while $R_{\text{c}}/R_{\text{c,vir}} \simeq 1.04 \pm 0.17$. Cores would appear to be sub-virial if their masses have been overestimated. For $M_{\text{c,min}}$, the sample has $\sigma_{\text{N}_2\text{D}^+}/\sigma_{\text{c,vir}} \simeq 1.21 \pm 0.16$, i.e. moderately super-virial, and $R_{\text{c}}/R_{\text{c,vir}} \simeq 3.40 \pm 0.56$. Cores would appear to have sizes larger than their predicted equilibrium sizes if their masses have been underestimated. Finally, for $M_{\text{c,mm}}$ the sample has $\sigma_{\text{N}_2\text{D}^+}/\sigma_{\text{c,vir}} \simeq 0.806_{0.707}^{0.964}$ and $R_{\text{c}}/R_{\text{c,vir}} \simeq 1.58_{1.30}^{2.08}$. Given the estimated uncertainties, we conclude that the sample of cores, with masses estimated from mm continuum emission, have properties broadly consistent with the virial equilibrium predictions of the Turbulent Core Model. There is tentative evidence that the cores have velocity dispersions that are marginally sub-virial, but as we shall see this is degenerate with the assumed magnetic field strength in the cores. The core sizes appear to be slightly larger than the equilibrium size. We note that this result may be influenced by our, somewhat arbitrary, choice of defining the core size via the 3σ $\text{N}_2\text{D}^+(3-2)$ contour.

Focusing on the most massive core, C1-S, with $M_{\text{c,mm}} \sim 62.5_{26.8}^{129} M_{\odot}$, we find that $\sigma_{\text{N}_2\text{D}^+}/\sigma_{\text{c,vir,mm}} \simeq 0.453_{0.327}^{0.652}$ and $R_{\text{c}}/R_{\text{c,vir,mm}} \simeq 0.994_{0.578}^{1.60}$. This may indicate that the core is quite strongly sub-virial, and so should be undergoing fairly rapid global collapse (its free-fall time is only $\sim 50,000$ years - Table 3). Alternatively, the core could be closer to virial equilibrium and supported by stronger large-scale magnetic fields than are assumed in the fiducial Turbulent Core Accretion model.

The assumed fiducial value of the Alfvén Mach number $m_A = \sqrt{3}\sigma_{\text{c}}/v_A = \sqrt{3}\sigma_{\text{c}}/(B/\sqrt{4\pi\rho_{\text{c}}}) = 1$ implies a mean background field strength in a core of

$$B_{\text{c}} = \sqrt{12\pi\rho_{\text{c}}\sigma_{\text{c}}m_A^{-1}} = 297m_A^{-1} \left(\frac{n_{\text{H,c}}}{10^5 \text{ cm}^{-3}} \right)^{1/2} \left(\frac{\sigma_{\text{c}}}{\text{km s}^{-1}} \right) \mu\text{G}. \quad (10)$$

In Table 3 we summarize the dynamical properties of the cores (based on the mm continuum core masses, the BTK extinction map for C1-N & S, and the far distance for IRDC F), including B_{c} for $m_A = 1$, evaluated using eq. 10 with $\sigma_{\text{c}} = \sigma_{\text{N}_2\text{D}^+}$. These values are $\sim 100 - 300 \mu\text{G}$.

To assess what field strength would be required for the core to be in virial equilibrium with $\sigma_{\text{N}_2\text{D}^+}/\sigma_{\text{c,vir,mm}} = 1$, note that $\sigma_{\text{c,vir,mm}} \propto \phi_B^{-3/8}$ (this assumes that the same value of ϕ_B applies in the clump envelope, which influences $\phi_{\bar{P}}$, as in the core). Thus in the case of C1-S, where $\sigma_{\text{N}_2\text{D}^+}/\sigma_{\text{c,vir,mm}} = 0.453$ (i.e. with $\phi_B = 2.8$), virial equilibrium would require $(\phi_{\text{B,vir}}/2.8)^{-3/8} = 0.453$, i.e. $\phi_{\text{B,vir}} = 23.1$, corresponding to $m_{\text{A,vir}} = 0.262$ and $B_{\text{c,vir}} = 1050 \mu\text{G}$. Analogous results for all the cores are shown in Table 3. For the cores that appear to be sub-virial in the fiducial analysis, a moderately stronger background magnetic field (by factors of a few) is required for virial equilibrium. Note that the ratio of $R_{\text{c}}/R_{\text{c,vir}}$ is only weakly affected by a change in ϕ_B , but stronger large-scale magnetic field support should lead to increased flattening of the core along the direction parallel to the field lines.

Could the masses of the observed cores be set by their magnetic field strengths? For an ellipsoidal core of length $2Z_{\text{c}}$ along the symmetry axis and radius R_{c} normal to the axis, the magnetic critical mass, i.e. the maximum mass that can

TABLE 2
IDENTIFIED N₂D⁺ CORES

Core property (% error)	C1-N	C1-S	F1	F2	G2-N	G2-S	Average
l ($^{\circ}$)	28.32503	28.32190	34.41923	34.43521	34.78097	34.77838	...
b ($^{\circ}$)	0.06724	0.06745	0.24598	0.24149	-0.56808	-0.56829	...
θ_c ($''$)	3.38	3.61	2.49	1.87	3.67	2.31	...
e	0.771	0.214	0.794	0.666	0.706	0.583	...
P.A. ($^{\circ}$)	-40	77	115	111	135	66	...
d (kpc) (20%)	5.0	5.0	3.7 (1.56) ^b	3.7 (1.56) ^b	2.9	2.9	...
R_c (0.01 pc) (20%)	8.18	8.75	4.46 (1.88)	3.35 (1.41)	5.16	3.25	...
$V_{\text{LSR},\text{N}_2\text{D}^+}$ (km s ⁻¹)	81.18±0.03	79.40±0.01	56.12±0.01	57.66±0.04	41.45±0.01	41.80±0.01	...
$\sigma_{\text{N}_2\text{D}^+, \text{obs}}$ (km s ⁻¹)	0.367±0.032	0.365±0.016	0.172±0.011	0.376±0.047	0.288±0.013	0.240±0.015	...
$\sigma_{\text{N}_2\text{D}^+, \text{nt}}$ (km s ⁻¹)	0.363±0.032	0.361±0.016	0.164±0.012	0.372±0.047	0.283±0.013	0.234±0.015	...
$\sigma_{\text{N}_2\text{D}^+}$ (km s ⁻¹)	0.409±0.031	0.407±0.019	0.250±0.021	0.417±0.044	0.340±0.018	0.300±0.020	...
$V_{\text{LSR},\text{DCO}^+}$ (km s ⁻¹)	81.18±0.02	79.59±0.02	56.26±0.01	57.53±0.02	41.52±0.01	41.91±0.02	...
$\sigma_{\text{DCO}^+, \text{obs}}$ (km s ⁻¹)	0.452±0.021	0.422±0.019	0.233±0.004	0.513±0.017	0.285±0.012	0.266±0.016	...
Σ_{cl} (g cm ⁻²) (30%)	0.340 [0.525] ^a	0.289 [0.442] ^a	0.217	0.324	0.214	0.194	...
$\Sigma_{\text{c,max}}$ (g cm ⁻²) (30%)	0.369 [0.609]	0.326 [0.514]	0.248	0.355	0.225	0.212	...
$M_{\text{c,max}}$ (M_{\odot}) (50%)	37.1 [61.3]	37.5 [59.2]	7.41 (1.32)	5.97 (1.06)	9.01	3.36	...
$n_{\text{H,c,max}}$ (10 ⁵ cm ⁻³) (36%)	4.68 [7.73]	3.87 [6.10]	5.78 (13.7)	11.0 (26.1)	4.53	6.78	...
$\sigma_{\text{c,vir,max}}$ (km s ⁻¹)	0.739±0.22 [0.934±0.28]	0.711±0.21 [0.887±0.26]	0.441±0.13 (0.287±0.085)	0.462±0.14 (0.300±0.089)	0.462±0.14	0.352±0.10	...
$\sigma_{\text{N}_2\text{D}^+}/\sigma_{\text{c,vir,max}}$	0.554±0.17 [0.438±0.13]	0.573±0.17 [0.459±0.14]	0.565±0.17 (0.871±0.27)	0.902±0.28 (1.39±0.44)	0.736±0.22	0.853±0.26	0.697±0.088 [0.659±0.085] ([0.791±0.11])
$R_{\text{c,vir,max}}$ (0.01 pc)	7.74±2.6 [8.00±2.7]	8.44±2.9 [8.57±2.9]	4.33±1.5 (1.82±0.62)	3.18±1.1 (1.34±0.46)	4.81±1.6	3.08±1.0	...
$R_c/R_{\text{c,vir,max}}$	1.06±0.42 [1.02±0.40]	1.04±0.41 [1.02±0.40]	1.03±0.41	1.05±0.41	1.07±0.42	1.05±0.42	1.05±0.17 [1.04±0.17]
$\Sigma_{\text{c,min}}$ (g cm ⁻²) (30%)	0.029 [0.084]	0.037 [0.072]	0.031	0.031	0.011	0.018	...
$M_{\text{c,min}}$ (M_{\odot}) (50%)	2.92 [8.45]	4.26 [8.29]	0.926 (0.165)	0.522 (0.0927)	0.44	0.286	...
$n_{\text{H,c,min}}$ (10 ⁵ cm ⁻³) (36%)	0.368 [1.07]	0.439 [0.854]	0.722 (1.71)	0.962 (2.28)	0.221	0.575	...
$\sigma_{\text{c,vir,min}}$ (km s ⁻¹)	0.391±0.12 [0.569±0.17]	0.413±0.12 [0.542±0.16]	0.262±0.078 (0.170±0.050)	0.251±0.074 (0.163±0.048)	0.217±0.064	0.190±0.056	...
$\sigma_{\text{N}_2\text{D}^+}/\sigma_{\text{c,vir,min}}$	1.05±0.32 [0.719±0.22]	0.986±0.30 [0.751±0.22]	0.951±0.29 (1.46±0.45)	1.66±0.52 (2.56±0.80)	1.57±0.47	1.58±0.48	1.30±0.17 [1.21±0.16] ([1.44±0.20])
$R_{\text{c,vir,min}}$ (0.01 pc)	2.17±0.74 [2.97±1.0]	2.84±0.97 [3.21±1.1]	1.53±0.52 (0.645±0.22)	0.940±0.32 (0.396±0.13)	1.06±0.36	0.899±0.31	...
$R_c/R_{\text{c,vir,min}}$	3.77±1.5 [2.75±1.1]	3.08±1.2 [2.73±1.1]	2.91±1.1	3.56±1.4	4.86±1.9	3.61±1.4	3.63±0.59 [3.40±0.56]
$S_{1.34\text{mm}}$ (mJy)	6.94±0.72	26.7±0.77	5.08±0.63	3.70±0.30	3.08±0.48	1.05±0.31	...
$S_{1.34\text{mm}}/\Omega$ (MJy/sr)	8.25±0.86	27.7±0.80	11.1±1.4	14.4±1.2	3.10±0.48	2.66±0.79	...
$\Sigma_{\text{c,mm}}$ (g cm ⁻²)	0.161 ^{0.321} _{0.0938}	0.542 ^{1.08} _{0.322}	0.218 ^{0.434} _{0.125}	0.282 ^{0.560} _{0.165}	0.0605 ^{0.121} _{0.0342}	0.0521 ^{0.106} _{0.0260}	...
$M_{\text{c,mm}}$ (M_{\odot})	16.2 ^{33.6} _{6.83}	62.5 ¹²⁹ _{26.8}	6.51 ^{13.5} _{2.71} (1.16 ^{2.40} _{0.482})	4.74 ^{9.80} _{1.74} (0.842 ^{1.04} _{0.358})	2.42 ^{5.03} _{0.992}	0.826 ^{1.74} _{0.296}	...
$n_{\text{H,c,mm}}$ (10 ⁵ cm ⁻³)	2.05 ^{4.12} _{1.10}	6.43 ^{12.9} _{3.52}	5.07 ^{10.2} _{2.69} (12.0 ^{24.2} _{6.35})	8.74 ^{17.6} _{4.72} (20.7 ^{11.7} _{1.7})	1.22 ^{2.46} _{0.635}	1.67 ^{3.41} _{0.766}	...
$\sigma_{\text{c,vir,mm}}$ (km s ⁻¹)	0.601 ^{0.828} _{0.418} [0.670 ^{0.923} _{0.468}]	0.808 ^{1.11} _{0.563} [0.899 ^{1.24} _{0.626}]	0.427 ^{0.589} _{0.297} (0.277 ^{0.383} _{0.193})	0.436 ^{0.601} _{0.304} (0.283 ^{0.390} _{0.197})	0.333 ^{0.459} _{0.231}	0.248 ^{0.343} _{0.171}	...
$\sigma_{\text{N}_2\text{D}^+}/\sigma_{\text{c,vir,mm}}$	0.681 ^{0.468} _{0.487} [0.611 ^{0.882} _{0.437}]	0.504 ^{0.725} _{0.364} [0.453 ^{0.652} _{0.327}]	0.584 ^{0.845} _{0.416} (0.899 ^{1.30} _{0.641})	0.956 ^{1.39} _{0.675} (1.47 ^{2.13} _{1.04})	1.02 ^{1.48} _{0.736}	1.21 ^{1.77} _{0.865}	0.826 ^{0.986} _{0.725} [0.806 ^{0.964} _{0.707}] ([0.944 ^{1.13} _{0.826}])
$R_{\text{c,vir,mm}}$ (0.01 pc)	5.12 ^{8.10} _{3.22} [4.12 ^{6.52} _{2.59}]	10.9 ^{17.2} _{6.90} [8.80 ^{13.9} _{5.58}]	4.06 ^{6.42} _{2.55} (1.71 ^{2.71} _{1.07})	2.83 ^{4.48} _{1.79} (1.19 ^{1.89} _{0.754})	2.49 ^{3.95} _{1.56}	1.53 ^{2.44} _{0.925}	...
$R_c/R_{\text{c,vir,mm}}$	1.60 ^{2.39} _{0.929} [1.99 ^{3.22} _{1.15}]	0.804 ^{1.30} _{0.468} [0.994 ^{1.60} _{0.578}]	1.10 ^{1.79} _{0.638}	1.18 ^{1.91} _{0.687}	2.07 ^{3.38} _{1.20}	2.12 ^{3.58} _{1.22}	1.48 ^{1.89} _{1.21} [1.58 ^{2.08} _{1.30}]

^aProperties derived from BTK MIR extinction map for C1-N & S, including sample averages, are shown inside “[...]”.

^bProperties derived assuming the 1.56 kpc distance estimate to IRDC F (Kurayama et al. 2011), including sample averages, are shown inside “(...)”.

be supported by a magnetic field, $B_{c,\text{crit}}$, is (Bertoldi & McKee 1992)

$$M_{c,B} = 1.62 \left(\frac{R_c}{Z_c} \right)^2 \left(\frac{B_{c,\text{crit}}}{100 \mu\text{G}} \right)^3 \left(\frac{n_{\text{H},c}}{10^5 \text{cm}^{-3}} \right)^{-2} M_{\odot}. \quad (11)$$

If we equate $M_{c,B} = M_{c,\text{mm}}$ for our cores (assuming $R_c = Z_c$), we can estimate the values of $B_{c,\text{crit}}$ that apply to their particular masses and densities. We find that these values are similar to $B_{c,\text{vir}}$ for all six cores, even though there is a range of required Alfvén Mach numbers, $m_{A,\text{vir}}$ of a factor of about eight. If a moderate degree of flattening is assumed so that $R_c = 2Z_c$, then the estimates of $B_{c,\text{crit}}$ decrease by a factor of $(Z_c/R_c)^{2/3} \rightarrow 0.63$ (at fixed $n_{\text{H},c}$).

Unfortunately, it is difficult to observationally determine magnetic field strengths in IRDC cores and we do not have any direct constraints for these particular sources. Measurement of Zeeman splitting from molecules such as CN (Falgarone et al. 2008) require relatively strong lines, whereas the observed emission is typically quite weak. From 14 regions, with average density of $n_{\text{H}} = 9 \times 10^5 \text{cm}^{-3}$, Falgarone et al. derived a median value of the total field strength of $560 \mu\text{G}$. Such values are similar to those needed for our N_2D^+ cores to be in virial equilibrium. Our most massive core requires a moderately higher value (and at a slightly lower density), but since massive starless cores (that will form massive stars) are rare objects, it is quite possible they require relatively unusual (stronger) magnetic field strengths. The Falgarone et al. magnetic field strength measurements form part of a set that were used by Crutcher et al. (2010) to estimate a median field strength versus density relation

$$B_{\text{med}} \simeq 0.22 \left(\frac{n_{\text{H}}}{10^5 \text{cm}^{-3}} \right)^{0.65} \text{mG} \quad (n_{\text{H}} > 300 \text{cm}^{-3}), \quad (12)$$

with uniform distribution of values up to $2B_{\text{med}}$. This predicts a median field strength about 1.6 times stronger than the Falgarone et al. values. Applying this relation to the density of C1-S yields $B_{\text{med}} = 730 \mu\text{G}$, close (within $\sim 40\%$) to the value needed for virial equilibrium. Formally, about 30% of the Crutcher et al. uniform distribution of field strengths at this density would be strong enough to support the core, but the uncertainties associated with this estimate, which is also model dependent, are large.

Magnetic field morphology can be measured via dust continuum polarization, but there are large uncertainties in estimating field strengths via the Chandrasekhar-Fermi method. Relatively order magnetic field morphologies, and thus relatively strong fields strengths, have been claimed to be present around some massive protostars (e.g. Girart et al. 2009), which is additional indirect evidence that dynamically important fields are also present at the earlier, starless core stage.

Another effect to consider is the possibility that, if magnetic fields are dynamically important, the true velocity dispersions of the cores are underestimated by those observed in ionized species, such as N_2D^+ (Houde et al. 2000; Falceta-Gonçalves et al. 2010; Tilley & Balsara 2010). Observations of neutral species in the core are needed, but many species are likely to have frozen-out onto dust grain ice mantles (as discussed above, we did not detect DCN(3-2) or $^{13}\text{CS}(5-4)$ towards the cores). If co-spatial neutral species emission is observed to have a larger velocity dispersion this would be evidence in support of dynamically important B-fields.

The cores discussed in this paper are overdense structures, most likely driven to their current structure by their self-gravity. Thus there is a strong possibility they are still in a state of contraction, which would deviate from that of perfect

TABLE 3
DYNAMICAL PROPERTIES OF N_2D^+ CORES^a

Core property (% error)	C1-N	C1-S	F1	F2	G2-N	G2-S
R_c (0.01 pc) (20%)	8.18	8.75	4.46	3.35	5.16	3.25
$\sigma_{\text{N}_2\text{D}^+}$ (km s^{-1})	0.409 ± 0.031	0.407 ± 0.019	0.250 ± 0.021	0.417 ± 0.044	0.340 ± 0.018	0.300 ± 0.020
Σ_{cl} (g cm^{-2}) (30%)	0.525	0.442	0.217	0.324	0.214	0.194
$M_{c,\text{mm}}$ (M_{\odot})	$16.2^{33.6}_{6.83}$	$62.5^{129}_{26.8}$	$6.51^{13.5}_{2.71}$	$4.74^{9.80}_{2.01}$	$2.42^{5.03}_{0.992}$	$0.826^{1.74}_{0.296}$
$\alpha_c \equiv 5\sigma_{\text{N}_2\text{D}^+}^2 R_c / (GM_{c,\text{mm}})$ ^b	$0.981^{2.35}_{0.419}$	$0.270^{0.634}_{0.119}$	$0.496^{1.20}_{0.209}$	$1.433^{4.41}_{0.588}$	$2.867^{0.94}_{1.24}$	$4.13^{1.6}_{1.75}$
$n_{\text{H},c,\text{mm}}$ (10^5cm^{-3})	$2.05^{4.12}_{1.10}$	$6.43^{12.9}_{3.52}$	$5.07^{10.2}_{2.69}$	$8.74^{17.6}_{4.72}$	$1.22^{2.46}_{0.635}$	$1.67^{3.41}_{0.766}$
$t_{c,\text{ff}}$ (10^5yr) ^c	$0.962^{1.31}_{0.678}$	$0.542^{0.734}_{0.383}$	$0.611^{0.838}_{0.431}$	$0.465^{0.633}_{0.328}$	$1.25^{1.73}_{0.878}$	$1.07^{1.57}_{0.745}$
B_c (μG) ($m_A = 1$)	156^{223}_{112}	275^{390}_{202}	$115^{83.0}_{164}$	330^{574}_{234}	$94.4^{134}_{67.9}$	$92.0^{61.8}_{132}$
$R_{c,\text{vir},\text{mm}}$ (0.01 pc)	$4.12^{6.52}_{2.59}$	$8.80^{13.9}_{5.58}$	$4.06^{6.42}_{2.55}$	$2.83^{4.48}_{1.79}$	$2.49^{3.95}_{1.56}$	$1.53^{2.44}_{0.925}$
$R_c/R_{c,\text{vir},\text{mm}}$	$1.99^{3.22}_{1.15}$	$0.994^{1.60}_{0.378}$	$1.10^{1.79}_{0.538}$	$1.18^{1.91}_{0.687}$	$2.07^{3.38}_{1.20}$	$2.12^{3.58}_{1.22}$
$\sigma_{c,\text{vir},\text{mm}}$ (km s^{-1})	$0.670^{0.923}_{0.466}$	$0.899^{0.34}_{0.626}$	$0.427^{0.589}_{0.297}$	$0.436^{0.6801}_{0.304}$	$0.333^{0.439}_{0.231}$	$0.248^{0.343}_{0.171}$
$\sigma_{\text{N}_2\text{D}^+} / \sigma_{c,\text{vir},\text{mm}}$	$0.611^{0.882}_{0.437}$	$0.453^{0.652}_{0.327}$	$0.584^{0.845}_{0.416}$	$0.956^{1.39}_{0.675}$	$1.02^{1.48}_{0.736}$	$1.21^{1.77}_{0.865}$
$\phi_{B,\text{vir}}$	$10.4^{25.5}_{3.41}$	$23.1^{55.0}_{8.76}$	$11.8^{29.0}_{39}$	$3.16^{7.98}_{1.17}$	$2.64^{6.35}_{0.992}$	$1.68^{4.12}_{0.613}$
$m_{A,\text{vir}}$	$0.405^{0.758}_{0.249}$	$0.262^{0.448}_{0.167}$	$0.379^{0.697}_{0.233}$	$0.899^{0}_{0.474}$	$1.06^{0}_{0.545}$	$1.99^{0}_{0.729}$
$B_{c,\text{vir}}$ (μG)	385^{577}_{178}	1050^{790}_{161}	304^{534}_{141}	367^{734}_{9}	89.3^{181}_{0}	46.3^{129}_{0}
$B_{c,\text{crit}}$ (μG)	219^{178}_{134}	736^{1610}_{452}	296^{646}_{180}	382^{834}_{234}	$82.2^{180}_{49.7}$	$70.7^{156}_{40.7}$

^aBased on the mm continuum core masses, the BTK extinction map for C1-N & S, and the far distance for IRDC F.

^bVirial parameter (Bertoldi & McKee 1992).

^cCore free-fall time, $t_{c,\text{ff}} = [3\pi/(32G\rho_c)]^{1/2} = 1.38 \times 10^5 (n_{\text{H},c,\text{mm}}/10^5 \text{cm}^{-3})^{-1/2} \text{yr}$.

virial equilibrium. Signatures of infall, e.g. as traced via the asymmetric profiles of optically thick lines, need to be searched for. Models of collapsing cores, even if initial regulated by magnetic fields, do predict magnetically supercritical central regions (e.g., Ciolek and Mouschovias 1994).

3.5. Comparison to some previous studies

Csengeri et al. (2011) studied the dynamics of five massive protostellar cores (i.e. those that are already forming a protostar) in Cygnus-X, concluding that the velocity dispersions were smaller than the predicted MT03 values for a virialized core. They measured velocity dispersions from observations of $\text{H}^{13}\text{CO}^+(1-0)$ ($\sim 4''$ angular resolution; 0.13 km s^{-1} velocity resolution) and $\text{N}_2\text{H}^+(1-0)$ ($29''$ angular resolution; 0.13 km s^{-1} velocity resolution). They assumed a single value of $\Sigma_{\text{cl}} = 1.7 \text{ g cm}^{-2}$ based on mm continuum emission. The main differences compared to our present study include: (1) they studied cores that are already forming stars; (2) they did not use deuterated species to trace the core gas; (3) they measured clump properties via mm continuum emission, rather than MIR extinction mapping.

Pillai et al. (2011) studied the dynamics of cold cores in the vicinity of ultracompact HII regions, also concluding they were strongly sub-virial. They used NH_2D emission ($\sim 4.5''$ angular resolution; 0.27 km s^{-1} velocity resolution) to measure velocity dispersion and 3.5 mm continuum emission to estimate mass. The main differences compared to our present study include: (1) Many of their cores are unresolved, with estimated deconvolved sizes that are much smaller than the angular resolution of their observations - yet all mm emission, i.e. mass, is assumed to originate from inside these effective radii. On the other hand, all of our cores are resolved. (2) No allowance was made for surface pressure terms in the consideration of virial equilibrium.

4. CONCLUSIONS

We used ALMA Cycle 0 observations to search for $\text{N}_2\text{D}^+(3-2)$ emission from four IRDCs, selected to be dark at wavelengths as long as $70 \mu\text{m}$. Strong detections were made in all cases, leading to identification of 6 N_2D^+ cores. We assessed their properties, including their surrounding clump envelopes, via MIR extinction maps. We also measured core masses via the detected 1.34 mm dust continuum emission. We regard this mass estimate as the most accurate for the cores (even though it still shows factor of 2 uncertainties), because of the difficulty of separating out core from clump material in the MIREX-derived mass surface density maps. The MIREX maps do, however, allow us to estimate the clump envelope properties, which are needed for the surface pressure term in the virial equation.

We assessed the dynamical state of the cores by comparing to the Turbulent Core Model of MT03. For the sample of 6 cores the ratio of the observed to the predicted (virial equilibrium) velocity dispersion is $0.81_{0.71}^{0.96}$, while the ratio of the observed to predicted size is $1.58_{1.30}^{2.08}$. Note, these error intervals assume random errors amongst the six cores, but if there are correlated systematic errors, e.g. in mass estimates, then the true error range could be larger. Thus, given the uncertainties, the cores appear to be quite close to the predictions of the model, which assumes virial and pressure equilibrium and invokes magnetic fields such that the Alfvén Mach number is $m_A = 1$. There is tentative evidence that the cores are slightly sub-virial compared to the fiducial model, especially in the case of the more massive cores C1-S and C1-N, with $\sim 63 M_\odot$ and $\sim 16 M_\odot$, respectively. However, these cores could be close to virial equilibrium if they are threaded by moderately stronger large-scale background magnetic fields with strengths up to $\sim 1 \text{ mG}$, implying that $m_A \simeq 0.3 - 0.4$.

To prevent fragmentation of the cores requires similar field strengths, which we have evaluated by equating observed core mass with the magnetic critical mass given its observed density. This may indicate that magnetic fields are dynamically important in setting the mass function of cores, as has been suggested by Kunz & Mouschovias (2009) (see also Bailey & Basu 2013), especially preventing the fragmentation of the massive cores that eventually form massive stars. Magnetic suppression of fragmentation appears to be the most likely mechanism operating in IRDCs, since the cold temperatures ($\sim 10 \text{ K}$) indicate that strong radiative heating from surrounding protostars to raise the thermal Jeans mass (Krumholz & McKee 2008) is not occurring. Magnetically mediated massive star formation would not require a minimum mass surface density threshold, such as the $\Sigma_{\text{cl}} \simeq 1 \text{ g cm}^{-2}$ limit proposed by Krumholz & McKee. Indeed the clump medium immediately surrounding C1-N and C1-S only has $\Sigma_{\text{cl}} \simeq 0.5 \text{ g cm}^{-2}$ and the clumps in the IRDC sample of BT12 tend to have even lower values.

This pilot study with ALMA revealed two relatively massive starless cores out of a total sample of six detected objects. Further observations of other regions are needed to build a larger statistical sample. Observations to constrain the magnetic field strengths in these objects are also needed.

We thank Gary Fuller, Jouni Kainulainen, Wanggi Lim, Chris McKee, Andy Pon and Scott Schnee for helpful discussions, as well as the comments of an anonymous referee. JCT acknowledges support from NSF CAREER grant AST-0645412; NASA Astrophysics Theory and Fundamental Physics grant ATP09-0094; NASA Astrophysics Data Analysis Program ADAP10-0110. SK acknowledges support from an NRAO-SOS grant in support of ALMA-Cycle 0 observations. This paper makes use of the following ALMA data: ADS/JAO.ALMA#2011.0.00236.S. ALMA is a partnership of ESO (representing its member states), NSF (USA) and NINS (Japan), together with NRC (Canada) and NSC and ASIAA (Taiwan), in cooperation with the Republic of Chile. The Joint ALMA Observatory is operated by ESO, AUI/NRAO and NAOJ. The National Radio Astronomy Observatory is a facility of the National Science Foundation operated under cooperative agreement by Associated Universities, Inc.

REFERENCES

- Bailey, N. D. & Basu, S. 2013, *ApJ*, 766, 27
- Benjamin, R. A., Churchwell, E. B., Babler, B. L. et al. 2003, *PASP*, 115, 953
- Bernard, J.-Ph., Paradis, D., Marshall, D. J. et al. 2010, *A&A*, 518, L88
- Bertoldi, F., & McKee, C. F. 1992, *ApJ*, 395, 140
- Bonnell, I. A., Clarke, C. J., Bate, M. R. et al. 2001, *MNRAS*, 324, 573
- Butler M. J., & Tan J. C. 2009, *ApJ*, 696, 484 (BT09)
- Butler M. J., & Tan J. C. 2012, *ApJ*, 754, 5 (BT12)
- Butler M. J., Tan J. C. & Käinulainen, J. 2013, *ApJ*, submitted (BTK)
- Carey, S. J., Noriega-Crespo, A., Mizuno, D. R. et al. 2009, *PASP*, 121, 76
- Caselli, P., Walmsley C. M., Tafalla M. et al. 1999, *ApJL*, 523, L165
- Caselli, P., Walmsley C. M., Zucconi A. et al. 2002, *ApJ*, 565, 344
- Ciolek, G. E. & Mouschovias, T. Ch. 1994, *ApJ*, 425, 142
- Crapsi, A., Caselli, P., Walmsley, M. C. et al. 2007, *A&A*, 470, 221
- Crutcher, R. M., Wandelt, B., Heiles, C. et al. 2010, *ApJ*, 725, 466
- Csengeri, T., Bontemps, S., Schneider, N. et al. 2011, *A&A*, 527, 135
- Dalgarno, A. & Lepp, S. 1984, *ApJ*, 287, L47
- Draine, B. T. 2011, *Physics of the Interstellar and Intergalactic Medium* (Princeton, NJ: Princeton Univ. Press)
- Egan, M. P., Shipman, R. F., Price, S. D., et al. 1998, *ApJ*, 494, L199
- Falceta-Gonçalves, D., Lazarian, A., & Houde, M. 2010, *ApJ*, 713, 1376
- Falgarone, E., Troland, T. H., Crutcher, R. M. et al. 2008, *A&A*, 487, 247
- Fontani, F., Giannetti, A., Beltrán, M. T. et al. 2012, *MNRAS*, 423, 2342
- Fontani, F., Palau, A., Caselli, P. et al. 2011, *A&A*, 529, L7
- Foster, J. B., Stead, J. J., Benjamin, R. A., et al. 2012, *ApJ*, 751, 157
- Girart, J. M., Beltrán, M. T., Zhang, Q. et al. 2009, *Science*, 324, 1408
- Hernandez, A. K., & Tan, J. C., Caselli, P. et al. 2011, *ApJ*, 738, 11
- Houde, M., Bastien, P., Peng, R. et al. 2000, *ApJ*, 536, 857
- Krumholz, M. R. & McKee, C. F. 2008, *Nature*, 451, 1082
- Krumholz, M. R., McKee, C. F. & Klein, R. I. 2005, *Nature*, 438, 332
- Kunz, M. W. & Mouschovias, T. Ch. 2009, *MNRAS*, 399, L94
- Kurayama, T., Nakagawa, A., Sawada-Satoh, S., et al. 2011, *PASJ*, 63, 513
- Li, A., & Draine, B. T. 2001, *ApJ*, 554, 778
- McKee, C. F., & Tan, J. C. 2003, *ApJ*, 585, 850 (MT03)
- McLaughlin, D. E., & Pudritz, R. E. 1996, *ApJ*, 476, 750
- Ossenkopf, V., & Henning, T. 1994, *A&A*, 291, 943 (OH94)
- Pagani, L., Vastel, C., Hugo, E. et al. 2009, *A&A*, 494, 623
- Pérou, M., Omont, A., Simon, G., et al. 1996, *A&A*, 315, L165
- Peretto, N., Fuller G. A., Plume R. et al. 2010, *A&A*, 518, L98
- Pillai, T., Kauffmann, J., Wyrowski, F. et al. 2011, *A&A*, 530, 118
- Pillai, T., Wyrowski, F., Carey, S. J. et al. 2006, *A&A*, 450, 569
- Shu, F. H., Adams, F. C., & Lizano, S. 1987, *ARA&A*, 25, 23
- Simon, R., Rathborne, J. M., Shah, R. Y. et al. 2006, *ApJ*, 653, 1325
- Tilley, D. A., & Balsara, D. 2010, *MNRAS*, 406, 1201
- Wang, P., Li, Z.-Y., Abel, T. & Nakamura, F. 2010, *ApJ*, 709, 27
- Zhang, Q., Wang, Y., Pillai, T. et al. 2009, *ApJ*, 696, 268